nature materials

LETTERS

https://doi.org/10.1038/s41563-018-0035-3

Organic-based magnon spintronics

Haoliang Liu[1,3], Chuang Zhang[1,3], Hans Malissa[1,3], Matthew Groesbeck[1], Marzieh Kavand[1], Ryan McLaughlin[1], Shirin Jamali[1], Jingjun Hao[2], Dali Sun[1], Royce A. Davidson[2], Leonard Wojcik[1], Joel S. Miller[2], Christoph Boehme[1] and Z. Valy Vardeny[1]*

Magnonics concepts utilize spin-wave quanta (magnons) for information transmission, processing and storage. To convert information carried by magnons into an electric signal promises compatibility of magnonic devices with conventional electronic devices, that is, magnon spintronics[1]. Magnons in inorganic materials have been studied widely with respect to their generation[2,3], transport[4,5] and detection[6]. In contrast, resonant spin waves in the room-temperature organic-based ferrimagnet vanadium tetracyanoethylene (V(TCNE)$_x$ ($x \approx 2$)), were detected only recently[7]. Herein we report room-temperature coherent magnon generation, transport and detection in films and devices based on V(TCNE)$_x$ using three different techniques, which include broadband ferromagnetic resonance (FMR), Brillouin light scattering (BLS) and spin pumping into a Pt adjacent layer. V(TCNE)$_x$ can be grown as neat films on a large variety of substrates, and it exhibits extremely low Gilbert damping comparable to that in yttrium iron garnet. Our studies establish an alternative use for organic-based magnets, which, because of their synthetic versatility, may substantially enrich the field of magnon spintronics.

As the limitations of electrical circuitry are reached, advanced paradigms are needed to develop future generations of fast and reduced energy dissipation (less lossy) miniature information-processing devices. Nearly all existing electronic devices are based on controlling the electric charge dynamics by electric fields. Electrons also possess spin that gives them their magnetic properties. Spin-density fluctuations in magnetically ordered materials, such as ferromagnets (FMs), can propagate in the form of spin waves, that is, magnons. Magnon current may be generated by microwave (MW) irradiation under FMR conditions[3], on the application of a temperature gradient via the spin Seebeck effect (SSE)[8] or by an electric current[9]. Magnons can be detected by various means, such as antenna[2], the time-resolved magneto-optical Kerr effect[10], BLS spectroscopies[9] and caloritronic methods[11]. In addition, magnons in an FM layer can induce a pure-spin current in a Pt adjacent layer through the process of spin pumping, which subsequently may be detected electrically via the inverse spin Hall effect (ISHE)[6,12]. This process is the basis for the application avenue of magnon spintronics.

In the past few years, a widely used magnetic insulator for magnon spintronics has been yttrium iron garnet (YIG ($Y_3Fe_5O_{12}$)) due to its low Gilbert damping[1]. For example, a coherent magnon current has been efficiently converted into electric signal in a YIG/Pt bilayer[4]. Also, SSE was observed in YIG/Pt that stems from a non-coherent magnon current[13]. In addition, a magnon spintronics transistor has been successfully engineered based on YIG[14]. However, the YIG films used for such magnon spintronics devices are difficult to grow and process, because they need be epitaxially grown as single crystals at high temperature[15]. Organic-based magnets may be alternative magnetic insulator candidates, because of both the reduced spin–orbit coupling and the lack of electron-lattice scattering, which may drastically reduce the Gilbert damping (α). For example, V(TCNE)$_x$ with $x \approx 2$ (Fig. 1a), which is ferrimagnetically ordered, exhibits a very narrow FMR linewidth in either powder or thin-film forms[16,17], and shows robust long-range magnetic order even in the absence of long-range structural order[18]. In addition, uniform perpendicular standing spin-wave modes have been identified in V(TCNE)$_x$ thin films; also, this magnet compound has been incorporated into a MW circuit[7]. We measured the electrical conductivity, σ, in V(TCNE)$_x$ films and found it to be $\sim 10^{-6}$ S cm^{-1} (Supplementary Fig. 1), and thus we consider this compound to be a magnetic insulator that may replace YIG. The broad variation in the reported conductivity value, as well as the transition temperature, T_c, for V(TCNE)$_x$ films is attributed to different growth conditions in different laboratories[17,19].

The magnetic order in V(TCNE)$_x$ originates from a three-dimensional antiferromagnetic exchange coupling between the V^{II} and the (TCNE) ion spins[20]. All of the spins in V^{II} ions and (TCNE)$^-$ anions are collinearly antiferromagnetically aligned (Fig. 1a), which results in a net magnetic moment of $\sim 1\,\mu_B$. V(TCNE)$_x$ can be synthesized from solution as powders, or films grown by chemical vapour deposition (CVD); the latter method leads to a significant increase of the structural order and to a less-prominent magnetic glassy behaviour[19,20]. Moreover, unlike YIG, high-quality V(TCNE)$_x$ thin films have been grown successfully on various substrates[19,21], with CVD-deposited thin films showing FMR responses with linewidths as narrow as that in YIG[16,17]. In addition, spin-aligned carrier injection from V(TCNE)$_x$ films was detected in spin–valve spintronic devices[21,22]. However, the impedance mismatch between the magnetic electrodes and the non-magnetic spacer layer in spin–valve devices limits the spin-injection efficiency[23,24]. In contrast, for spin pumping under FMR conditions and subsequent ISHE detection, the impedance mismatch is circumvented[25–29]. This was recently shown for organic semiconductors by demonstrating the ISHE in several organic films with various spin–orbit couplings, using both NiFe and YIG magnetic spin-pumping substrates[26,29].

The CVD-deposited V(TCNE)$_x$ thin films were grown from the reaction of TCNE and V(CO)$_6$ (ref. [19]) on glass templates that have lithographically defined Cu electrodes, and a Pt stripe for ISHE detection (Methods). The samples were investigated using superconducting quantum interference device (SQUID) magnetometry to confirm their magnetic order above room temperature (Fig. 1b), which reveals a transition temperature, T_c, of ~370 K (Fig. 1b). However, the reduction of the magnetic order at T_c may be partially due to the onset of a structure rearrangement in the V(TCNE)$_x$

[1]Department of Physics & Astronomy, University of Utah, Salt Lake City, UT, USA. [2]Department of Chemistry, University of Utah, Salt Lake City, UT, USA. [3]These authors contributed equally: Haoliang Liu, Chuang Zhang, Hans Malissa. *e-mail: val@physics.utah.edu

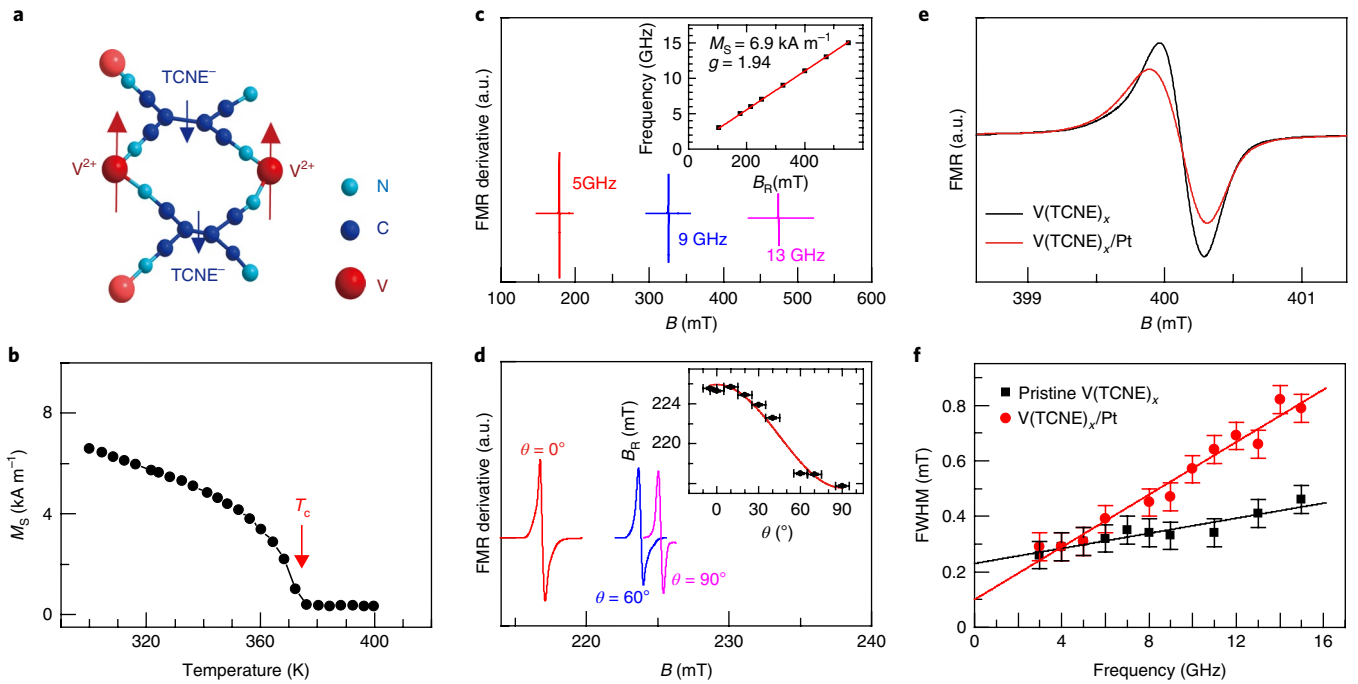

Fig. 1 | FMR in V(TCNE)$_x$ films. a, The magnetic structure of V(TCNE)$_x$. The V^{2+} and $(TCNE)^-$ spins interact via direct coupling. **b**, The temperature dependence of the saturation magnetization, M_S, in a ~220 nm thick V(TCNE)$_x$ film measured with SQUID magnetometry with an in-plane magnetic field of 100 mT (at saturation conditions). The transition temperature, T_c, is ~370 K. **c**, FMR(B) derivative spectra measured at various MW frequencies at room temperature. The inset shows the frequency dependence of the resonance field, B_R. The line through the data points is a fit using the Kittel equation (see text) from which M_S and the g-factor are obtained. **d**, FMR(B) spectra measured at $\nu = 6$ GHz and various angles, θ, of the applied magnetic field with respect to the film normal. The inset shows the angular dependence of B_R. The experimental uncertainties originate from the resolution of the rotation steps. The solid line through the data represents a fit using the values of M_S and g-factor in **c**. **e**, The FMR(B) spectra close to $B = B_R$ in pristine V(TCNE)$_x$ film and a V(TCNE)$_x$/Pt bilayer at $\nu = 11$ GHz. The linewidth in the bilayer structure is broadened. **f**, The MW-frequency dependence of the FMR linewidth for pristine V(TCNE)$_x$ and a V(TCNE)$_x$/Pt bilayer, from which the Gilbert damping factor, α, can be obtained (see text). Extrapolating the fitted straight lines to $\nu = 0$, we conclude that the smaller extrapolated linewidth for the V(TCNE)$_x$/Pt bilayer indicates a better inhomogeneity for the V(TCNE)$_x$ films grown on Pt, as compared with the films deposited on a glass substrate. The experimental uncertainties in **c** and **f** stem from the magnet field strength, which was calibrated by a Gauss meter. a.u., arbitrary units.

film[19], and thus the critical temperature for magnetic order may be much higher, as obtained using the Bloch law fitting[17]. Figure 1c shows broadband FMR(B) derivative spectrum (B is the external magnetic field strength) at various MW frequencies, ν. The narrow peak-to-peak width, ΔB of ~0.3 mT at 11 GHz (Fig. 1e) indicates good film homogeneity. We determined the Gilbert damping, α of the V(TCNE)$_x$ film from the slope of the FMR linewidth versus frequency, which reads $\Delta B = \Delta B_0 + \frac{4\pi\alpha\nu}{\sqrt{3}\gamma}$ (Fig. 1f), where ΔB_0 denotes a inhomogeneous broadening by structural imperfections and γ is the gyromagnetic factor. ΔB_0 is ~0.1 mT larger for V(TCNE)$_x$ grown on glass than on Pt, which indicates a better homogeneity for the V(TCNE)$_x$ grown on Pt. From our broadband FMR measurements, we obtained $\alpha = 3.2 \times 10^{-4}$, which is close to $\alpha = 2.3 \times 10^{-4}$ measured in YIG thin films[2]. The small α value indicates that the generated magnons in V(TCNE)$_x$ have very low losses, which is a prerequisite for magnon-based spintronic applications.

The MW-frequency dependence of the resonance field, B_R (Fig. 1c inset), can be accurately described using the Kittel equation[30], $\nu = \gamma/2\pi[B_R(B_R + \mu_0 M_S)]^{1/2}$, where M_S is the saturation magnetization. From the fit to the experimental data, we obtain the parameters $g = 1.94$ and $M_S = 6.9$ kA m^{-1}. We also found that the FMR(B) response changes with the field orientation, θ (Fig. 1d), where θ denotes the angle between the field direction and film normal. The angular dependence of B_R (inset to Fig. 1d inset) can be also fit by the Kittel equation (Supplementary equation (1)) with the same g-factor and M_S values as in Fig. 1c, which confirms the magnetic nature of the V(TCNE)$_x$ film.

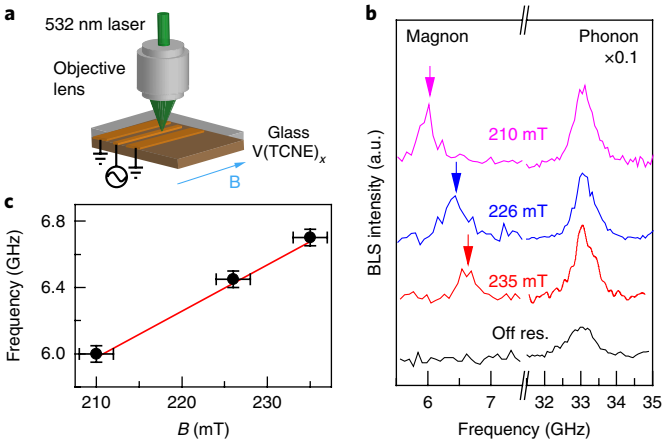

Fig. 2 | Magnon detection in a 520-nm-thick V(TCNE)$_x$ film using BLS spectroscopy at room temperature. a, Schematics of the BLS set-up to measure magnons under FMR conditions. **b**, BLS spectra measured at various magnetic fields and matched MW frequencies. The intensity of the phonon band is multiplied by a factor of 0.1 for ease of comparison. Here, res. stands for resonance. The arrows point to the magnon band frequency. **c**, The relation between the magnetic field and the obtained magnon BLS frequency. The experimental uncertainties were estimated from the magnetic field value and BLS interferometer resolutions. The line through the data points is a fit using the M_S and g-factor values in Fig. 1c.

To observe FMR-generated magnons directly in the V(TCNE)$_x$ film, BLS spectroscopy was performed. The BLS excitation laser beam was focused on the transmission line of a co-planar waveguide that was prepared on a glass substrate prior to V(TCNE)$_x$ film deposition (Fig. 2a), which guided the MW radiation close to the organic film that induces a MW magnetic field B_1 into the layer. The BLS spectrum was recorded under FMR conditions at various MW frequencies and matched magnetic fields (Fig. 2b); the overall resolution of the BLS set-up (including the spectrometer and laser bandwidth), $\delta\nu_0 \approx 0.5$ GHz. As seen, each BLS spectrum at resonance contains two bands at high and low energies. The high energy band at ~33 GHz is due to light scattering from acoustic phonons in the glass substrate; this band does not shift with the magnetic field. In contrast, the low-energy BLS band shifts with the field; thus, it is due to light scattering by the MW-generated magnons, which correspond to the uniform spin-wave mode (Supplementary equation (1)). As a control experiment, we checked that the magnon BLS band disappears when the MW frequency is off-resonance with B, which indicates that BLS from the thermal magnons in the V(TCNE)$_x$ film is below our noise level. The obtained relation between the measured BLS magnon frequency and the magnetic field is depicted in Fig. 2c, and is in agreement with the FMR relation seen in the Fig. 1c inset. Thus, the BLS data are direct proof for the presence of magnons in the V(TCNE)$_x$ film.

The magnon linewidth, $\delta\nu_m$, in the BLS spectrum may be used to estimate a lower limit of the magnon lifetime in the V(TCNE)$_x$ film. As seen in Fig. 2b, we measure $\delta\nu_m \approx 0.5$ GHz for the magnon BLS band, which is equal to the optical set-up resolution, $\delta\nu_0$. This indicates that the magnon intrinsic linewidth $\delta\nu_i < \delta\nu_0$ (otherwise we would have measured $\delta\nu_m > \delta\nu_0$). From this $\delta\nu_i$ upper limit we thus infer that the magnon lifetime is in the nanosecond time range. The acoustic phonon linewidth, $\delta\nu_{ac}$, in the glass substrate measured with the same set-up is $\delta\nu_{ac} \approx 2\delta\nu_0$ (which leads to a phonon lifetime in the range of a few hundred picoseconds), which corroborates the estimate for the $\delta\nu_i$ value made above.

The FMR linewidth for the MW-frequency range used here is broader in V(TCNE)$_x$/Pt bilayers compared with that of V(TCNE)$_x$

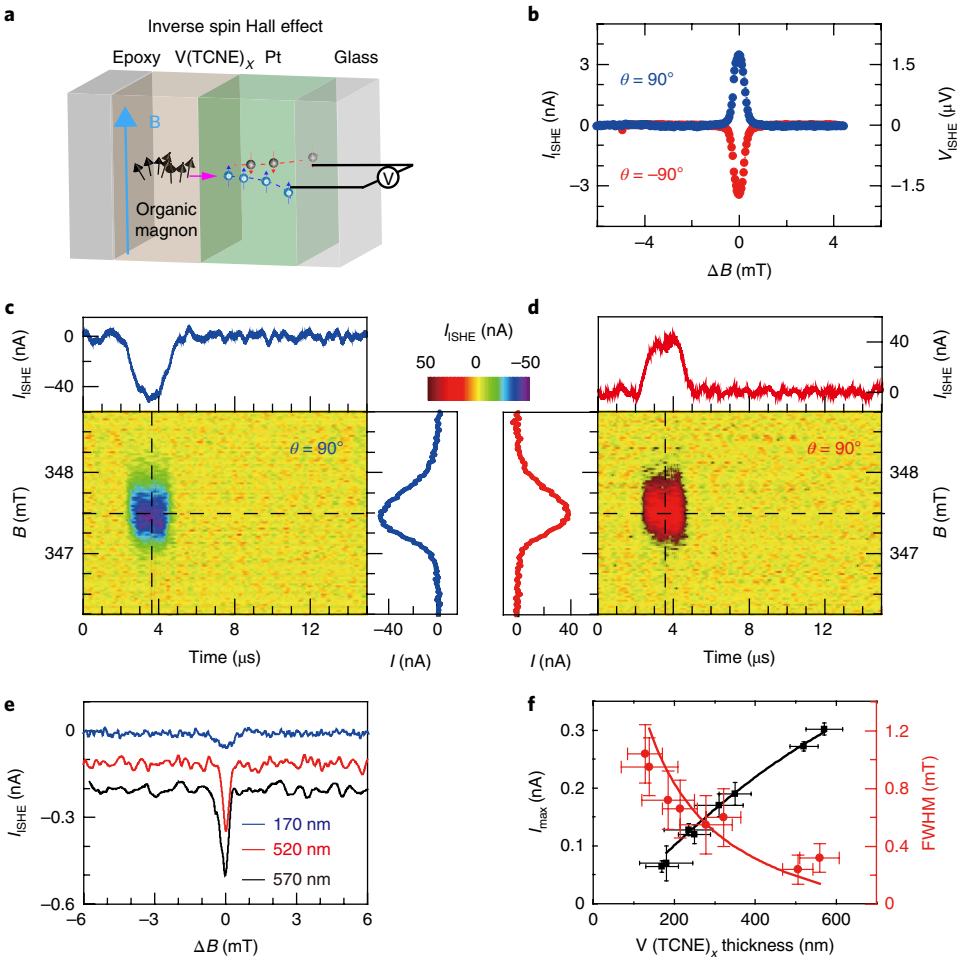

Fig. 3 | Observation of a FMR-driven ISHE in V(TCNE)$_x$/Pt bilayers using pulsed and continuous MW excitation. a, Schematic illustration of the conversion process of the magnon current in a V(TCNE) substrate into electric current in the Pt overlayer via the ISHE. **b**, The $I_{ISHE}(B)$ response close to $B = B_R$ using cw MW excitation at FMR conditions and $\nu = 3$ GHz measured in V(TCNE)$_x$ (8 μm)/Pt (7 nm) bilayer. The resistance of the device is ~500 Ω. **c**,**d**, Colour plots of I_{ISHE} as a function of B and time before, during and after a 2 μs long MW pulse is applied. The upper panels and lower right/left panels display the line profiles taken from the colour plot at the position of the horizontal and vertical dashed lines. The magnetic field polarity in **c** is opposite to that in **d**. The ISHE responses in panels **b**, **c** and **d** were measured in the same device. **e**, The cw $I_{ISHE}(B)$ response in V(TCNE)/Pt devices based on various V(TCNE)$_x$ film thicknesses, d. For better comparison, the three data sets are plotted with arbitrary offsets. **f**, The $I_{ISHE}(B)$ peak current (I_{max}) and its FWHM value plotted versus d. The thickness uncertainties were estimated from the average of three thickness measurements; whereas the ISHE uncertainties are due to uncertainty in the sample position WITH respect to the MW waveguide. The spin-mixing conductance, $g_{eff}^{\uparrow\downarrow}$, is obtained from the fit (red line) to the FWHM versus d data points, using Supplementary equation (5). The black line through the I_{max} versus d data points is a theoretical model based on the obtained $g_{eff}^{\uparrow\downarrow}$ value using Supplementary equation (2).

films grown on glass substrates (Fig. 1e), which indicates an excess magnon loss at the V(TCNE)$_x$/Pt interface. However, the excess loss is underestimated because the inhomogeneity-related ΔB_0 is smaller in V(TCNE)$_x$/Pt bilayers than in V(TCNE)$_x$/glass films. To eliminate the contribution of inhomogeneity broadening, the Gilbert damping factor α values obtained from the broadband FMR measurements are compared in Fig. 1f. The larger α value observed for FMR in V(TCNE)$_x$/Pt could originate from excess magnon loss compared with α values in V(TCNE)$_x$ films grown on glass, due to an enhanced scattering at the organic/Pt interface[31]. This suggests that the FMR-generated magnon current in the V(TCNE)$_x$ films efficiently transfers spin angular momentum at the interface to the Pt adjacent layer via spin pumping, which, in turn induces a spin current in the Pt adjacent layer. This assumption can be tested by generating a spin current in the Pt adjacent layer. This enables spin-current detection by conversion into charge current via the ISHE, as schematically displayed in Fig. 3a. For this experiment, the film normal to the magnetic field direction and the generated electric current must be perpendicular to each other.

To validate this scenario experimentally, we have conducted FMR-driven ISHE measurements using both continuous wave (cw) at $\nu = 3$ GHz and pulsed at $\nu = 9.63$ GHz MW frequency, as shown in Fig. 3b–d. As seen in Fig. 3b, the cw ISHE electric current response, $I_{\mathrm{ISHE}}(B)$, in the Pt adjacent layer shows a narrow band around the resonance field, $B_{\mathrm{R}} = 104$ mT; this reverses polarity when the field direction is reversed. These are the two crucial signatures of the ISHE in the non-magnetic adjacent layer. As a control experiment, we compared the cw ISHE response in bilayers of V(TCNE)$_x$/Pt and YIG/Pt using the same set-up and conditions, and found that the ISHE(B) response in the former bilayer is much narrower without compromising the strength (Supplementary Fig. 4c).

For the pulsed ISHE experiments in the V(TCNE)$_x$/Pt bilayer, short, homogeneous, high-power, low-duty cycle MW radiation was applied, and I_{ISHE} was monitored as function of time. This procedure excludes that continuous heating and gradient heating artefacts could affect the sample current[29]. Figure 3c,d shows colour plots of I_{ISHE} as a function of time and B for two geometrically opposite magnetic field orientations, θ, when a 2 µs long high-power MW pulse at frequency of 9.63 GHz is applied about 2 µs after the beginning of the pulse sequence. A significant I_{ISHE} occurs only during the MW pulse and for $B \approx B_{\mathrm{R}}$, where B_{R} corresponds to the FMR field of the V(TCNE)$_x$ substrate. Slice projections along the dashed lines are displayed in the plots above and between the colour plots. These show that I_{ISHE} also reverses polarity on reversing the field direction. In addition, we also see that the ISHE vanishes when the magnetic field is oriented perpendicular to the V(TCNE)$_x$ film (Supplementary Fig. 6). These are clear indications of spin-pumping-induced pure-spin current in the Pt adjacent layer.

Figure 3e displays three plots of $I_{\mathrm{ISHE}}(B)$ spectra of V(TCNE)$_x$/Pt devices of various organic film thicknesses, d, under a cw FMR drive. There is a substantial increase of I_{ISHE} with d. Figure 3f shows a plot of the current maximum, I_{max}, of $I_{\mathrm{ISHE}}(B)$ under cw FMR as a function of d. As seen, I_{max} increases with d; whereas the $I_{\mathrm{ISHE}}(B)$ linewidth, as determined by the full-width at half-maximum (FWHM), decreases with d. To describe the thickness dependence of I_{max} and FWHM, we employ a phenomenological model adopted from ISHE experiments in YIG/Pt bilayers[32]. The $I_{\mathrm{ISHE}}(B)$ linewidth, ΔB in this model, depends on d via: $\Delta B \sim \alpha_0 + \Delta\alpha_{\mathrm{sp}}\left(\approx \frac{g\mu_{\mathrm{B}}}{4\pi M_{\mathrm{S}} d} g_{\mathrm{eff}}^{\uparrow\downarrow}\right)$ (Supplementary equation (2)), where $g_{\mathrm{eff}}^{\uparrow\downarrow}$ is the spin-mixing conductance at the V(TCNE)$_x$/Pt interface, and α_0 of the pristine V(TCNE)$_x$ film is taken from Fig. 1f. From the fit of ΔB with d we thus obtain $g_{\mathrm{eff}}^{\uparrow\downarrow} = (0.95 \pm 0.12) \times 10^{18}$ m^{-2}. This $g_{\mathrm{eff}}^{\uparrow\downarrow}$ value is comparable to that in YIG[32]. Moreover, using the obtained $g_{\mathrm{eff}}^{\uparrow\downarrow}$ and the relation $I_{\mathrm{SHE}} \sim \theta_{\mathrm{SHE}}^{\mathrm{Pt}} \lambda_{\mathrm{S}}^{\mathrm{Pt}} B_1 g_{\mathrm{eff}}^{\uparrow\downarrow} \tanh\left(\frac{2d_{\mathrm{Pt}}}{\lambda_{\mathrm{S}}}\right)$ (Supplementary equations (3)–(5)) we can fit the $I_{\mathrm{max}}(d)$ dependence. Here $\lambda_{\mathrm{S}}^{\mathrm{Pt}}$ and $\theta_{\mathrm{SHE}}^{\mathrm{Pt}}$ are the Pt spin-diffusion length and spin Hall angle, respectively, and B_1 (= 0.01 mT) is the radiofrequency field. From the fit (Fig. 3f) and taking $\lambda_{\mathrm{S}}^{\mathrm{Pt}} = 1.5$ nm (ref. [29]), we obtain $\theta_{\mathrm{SHE}}^{\mathrm{Pt}} = 0.033 \pm 0.003$, which is within the range of $\theta_{\mathrm{SHE}}^{\mathrm{Pt}}$ values in the literature[33]. This agreement validates the spin-pumping process in the V(TCNE)$_x$/Pt bilayer.

In conclusion, we demonstrate resonantly generated magnons in thin films of the organic-based ferrimagnet insulator V(TCNE)$_x$, and subsequent efficient spin pumping by magnon scattering at the V(TCNE)$_x$/Pt interface. The FMR-generated magnons are observed directly by BLS, from which we estimate the magnon lifetime to be in the nanosecond time domain. Our experiments show that V(TCNE)$_x$ is a technologically easy-to-process organic-based magnetic thin-film insulator with an extremely low Gilbert damping, as needed for the development of magnonic devices. Combining V(TCNE)$_x$ magnon-current generation with ISHE-based organic spin-current detection could eventually lead to a class of all organic magnonic spintronics devices. This is significant, because the synthetic versatility and stability of organic magnetic compounds means our work opens a substantive avenue for their applications.

Methods

Methods, including statements of data availability and any associated accession codes and references, are available at https://doi.org/10.1038/s41563-018-0035-3.

Received: 21 September 2017; Accepted: 6 February 2018;
Published online: 12 March 2018

References

1. Chumak, A. V., Vasyuchka, V. I., Serga, A. A. & Hillebrands, B. Magnon spintronics. *Nat. Phys.* **11**, 453–461 (2015).
2. Collet, M. et al. Generation of coherent spin-wave modes in yttrium iron garnet microdiscs by spin–orbit torque. *Nat. Commun.* **7**, 10377 (2016).
3. Jungfleisch, M. B. et al. Large spin-wave bullet in a ferrimagnetic insulator driven by the spin Hall effect. *Phys. Rev. Lett.* **116**, 057601 (2016).
4. Kajiwara, Y. et al. Transmission of electrical signals by spin-wave interconversion in a magnetic insulator. *Nature* **464**, 262–266 (2010).
5. Cornelissen, L. J., Liu, J., Duine, R. A., Youssef, J. B. & van Wees, B. J. Long-distance transport of magnon spin information in a magnetic insulator at room temperature. *Nat. Phys.* **11**, 1022–1026 (2015).
6. Saitoh, E., Ueda, M., Miyajima, H. & Tatara, G. Conversion of spin current into charge current at room temperature: inverse spin-Hall effect. *Appl. Phys. Lett.* **88**, 182509 (2006).
7. Zhu, N. et al. Low loss spin wave resonances in organic-based ferrimagnet vanadium tetracyanoethylene thin films. *Appl. Phys. Lett.* **109**, 082402 (2016).
8. Bauer, G. E. W., Saitoh, E. & van Wees, B. J. Spin caloritronics. *Nat. Mater.* **11**, 391–399 (2012).
9. Demidov, V. E. et al. Magnetic nano-oscillator driven by pure spin current. *Nat. Mater.* **11**, 1028–1031 (2012).
10. Bauer, H. G., Chauleau, J. Y., Woltersdorf, G. & Back, C. H. Coupling of spinwave modes in wire structures. *Appl. Phys. Lett.* **104**, 102404 (2014).
11. An, T. et al. Unidirectional spin-wave heat conveyer. *Nat. Mater.* **12**, 549–553 (2013).
12. Mosendz, O. et al. Quantifying spin Hall angles from spin pumping: experiments and theory. *Phys. Rev. Lett.* **104**, 046601 (2010).
13. Uchida, K. et al. Spin Seebeck insulator. *Nat. Mater.* **9**, 894–897 (2010).
14. Chumak, A. V., Serga, A. A. & Hillebrands, B. Magnon transistor for all-magnon data processing. *Nat. Commun.* **5**, 4700 (2014).
15. Ellsworth, D. et al. Photo-spin-voltaic effect. *Nat. Phys.* **12**, 861–866 (2016).
16. Plachy, R. et al. Ferrimagnetic resonance in films of vanadium [tetracyanoethanide]$_x$, grown by chemical vapor deposition. *Phys. Rev. B* **70**, 064411 (2004).
17. Yu, H. et al. Ultra-narrow ferromagnetic resonance in organic-based thin films grown via low temperature chemical vapor deposition. *Appl. Phys. Lett.* **105**, 012407 (2014).
18. Miller, J. S. Oliver Kahn Lecture: Composition and structure of the V[TCNE]$_x$ (TCNE = tetracyanoethylene) room-temperature, organic-based magnet—a personal perspective. *Polyhedron* **28**, 1596–1605 (2009).
19. Pokhodnya, K. I., Epstein, A. J. & Miller, J. S. Thin-film V[TCNE]$_x$ magnets. *Adv. Mater.* **12**, 410–413 (2000).
20. Manriquez, J. M., Yee, G. T., McLean, R. S., Epstein, A. J. & Miller, J. S. A room-temperature molecular/organic-based magnet. *Science* **252**, 1415–1417 (1991).

21. Yoo, J.-W. et al. Spin injection/detection using an organic-based magnetic semiconductor. *Nat. Mater.* **9**, 638–642 (2010).
22. Fang, L. et al. Electrical spin injection from an organic-based ferrimagnet in a hybrid organic–inorganic heterostructure. *Phys. Rev. Lett.* **106**, 156602 (2011).
23. Xiong, Z. H., Wu, D., Valy Vardeny, Z. & Shi, J. Giant magnetoresistance in organic spin-valves. *Nature* **427**, 821–824 (2004).
24. Dediu, V. A., Hueso, L. E., Bergenti, I. & Taliani, C. Spin routes in organic semiconductors. *Nat. Mater.* **8**, 707–716 (2009).
25. Ando, K. et al. Electrically tunable spin injector free from the impedance mismatch problem. *Nat. Mater.* **10**, 655–659 (2011).
26. Ando, K., Watanabe, S., Mooser, S., Saitoh, E. & Sirringhaus, H. Solution-processed organic spin–charge converter. *Nat. Mater.* **12**, 622–627 (2013).
27. Watanabe, S. et al. Polaron spin current transport in organic semiconductors. *Nat. Phys.* **10**, 308–313 (2014).
28. Koopmans, B. Organic spintronics: pumping spins through polymers. *Nat. Phys.* **10**, 249–250 (2014).
29. Sun, D. et al. Inverse spin Hall effect from pulsed spin current in organic semiconductors with tunable spin-orbit coupling. *Nat. Mater.* **15**, 863–869 (2016).
30. Kittel, C. On the theory of ferromagnetic resonance absorption. *Phys. Rev.* **73**, 155–161 (1948).
31. Tserkovnyak, Y., Brataas, A. & Bauer, G. E. W. Enhanced Gilbert damping in thin ferromagnetic films. *Phys. Rev. Lett.* **88**, 117601 (2002).
32. Jungfleisch, M. B. et al. Thickness and power dependence of the spin-pumping effect in $Y_3Fe_5O_{12}$/Pt heterostructures measured by the inverse spin Hall effect. *Phys. Rev. B* **91**, 134407 (2015).
33. Rojas-Sánchez, J. C. et al. Spin pumping and inverse spin Hall effect in platinum: the essential role of spin-memory loss at metallic interfaces. *Phys. Rev. Lett.* **112**, 106602 (2014).

Acknowledgements

This work was supported by NSF grant no. DMR-1701427 (p-ISHE measurements), MURI-AFOSR grant FA9550-14-1-0037 (cw ISHE and FMR measurements) and NSF MRSEC grant no. DMR-1121252 (the $V(TCNE)_x$ synthesis and film growth). All the authors contributed to the preparation of the manuscript.

Author contributions

Z.V.V., C.B. and J.S.M. were responsible for the project planning, group management and final writing of the manuscript. H.L., C.Z., R.A.D., R.M. and J.H. prepared the organic magnetic films. H.L., C.Z., S.J. and D.S. prepared the ISHE devices. R.A.D. measured the critical temperature using SQUID. H.L., M.G. and D.S. measured the Gilbert damping and inverse spin Hall response using cw MW excitation. H.L. and C.Z. measured the non-thermal magnons using BLS. H.M. and M.K. measured the inverse spin Hall response by pulse MW. All the authors contributed to the results, analysis, discussion and manuscript preparation.

Competing interests

The authors declare no competing interests.

Additional information

Supplementary information is available for this paper at https://doi.org/10.1038/s41563-018-0035-3.

Reprints and permissions information is available at www.nature.com/reprints.

Correspondence and requests for materials should be addressed to Z.V.V.

Publisher's note: Publisher's note: Springer Nature remains neutral with regard to jurisdictional claims in published maps and institutional affiliations.

Methods

The $V(TCNE)_x$ thin films were prepared by CVD through the reaction between two precursors, namely TCNE and $V(CO)_6$. Optimized film deposition was achieved by keeping the TCNE and $V(CO)_6$ at 55 °C and 15 °C, respectively. Under these conditions, the obtained films showed a high magnetic order temperature, T_c (~370 K), relatively small saturation field and narrow FMR linewidth. The film thickness was determined by profilometry measurements (KLA Tencor). For the $V(TCNE)_x$/Pt bilayer device, prior to the $V(TCNE)_x$ film deposition, a 7 nm thick 0.7 × 3 mm Pt stripe was deposited on a glass substrate to detect the ISHE voltage. The resistance of the Pt layer was measured as ~500 Ω for all the ISHE devices. The electrodes were prepared by photolithographic means. The metal depositions were done by electron-beam evaporation at a base pressure of 10^{-7} mbar. As the $V(TCNE)_1$ film may degrade in air within ~2 h, it was necessary to encapsulate the films with an ultraviolet-cured epoxy (type E131 (Ossila Inc.)), which significantly increases the film lifetime to more than one month (Supplementary Fig. 9) if stored at low temperature[34]. The magnetic order temperature of the $V(TCNE)_x$ films was determined from measurements of the magnetization, M, as a function of temperature, T, at 100 mT using a Quantum Design MPMS-5 5 T SQUID magnetometer. The BLS experiments were performed using a Sandercock-type six-pass tandem Fabry–Perot interferometer in the backscattering geometry. The laser beam of 3 mW power was derived from a single-mode solid-state laser operated at 532 nm. The light beam was p-polarized and subsequently focused on the sample by JRS CM-1 microscopy. To enhance the magnon detection we measured the BLS spectrum under FMR conditions, in which the MW radiation was guided onto the $V(TCNE)_x$ film via a suitable co-planar waveguide, in which the excitation beam was focused in between the metal stripes. We measured both the Stokes and anti-Stokes light scattering from magnons and phonons, respectively. However, only the magnon BLS band shifted with the magnetic field. The broadband FMR measurements were performed at room temperature with a co-planar waveguide design. The MW radiation was generated using an Agilent N5173B generator operated in the frequency range of 9–20 GHz. For the FMR detection, we used a phase-sensitive scheme in which a weak magnetic field of 2 mT was modulated at 86 Hz in a Helmholtz coil between the poles of the d.c. magnet. For the cw ISHE measurements, the MW frequency was fixed at 3 GHz and the power was amplified using an amplifier (MINI-CIRCUITIS LAB Model ZHL-42). We used a phase-sensitive detection scheme to measure the induced electrical voltage on the Pt stripe, in which the excitation MW beam was amplitude modulated at 17 kHz. The pulsed ISHE was measured in a commercial EPR spectrometer (Bruker ElexSys E580). The transient ISHE response during the high-power MW excitation was amplified by a pre-amplifier (SR570 (Stanford Research Systems)) with the filter setting of the 100 Hz high-pass filter and a sensitivity of 20 uA V^{-1}, and recorded using the built-in digitizer of the spectrometer.

Data availability. The data that support the findings of this study are available from the corresponding author on reasonable request.

References

34. Froning, I. H. et al. Thin-film encapsulation of the air-sensitive organic-based ferrimagnet vanadium tetracyanoethylene. *Appl. Phys. Lett.* **106**, 122403 (2015).